



Cite this: DOI: 10.1039/d6lf00030d

Stable double gyroid network phases in asymmetric linear triblock amphiphiles

Daoyuan Li,^{ab} Mahesh K. Mahanthappa,^{id}^a
Timothy P. Lodge^{id}^{*ac} and J. Ilja Siepmann^{id}^{*abc}

Molecular dynamics simulations are employed to elucidate the phase behavior of a series of asymmetric linear triblock amphiphiles consisting of a sugar-based center segment (A_4) containing four hydroxyl groups with the ability to form inter- and intramolecular hydrogen bonds that is flanked by two nonpolar hydrocarbon segments (C_6H_{13} and C_xH_{2x+1} , denoted as B_6 and B_x with $6 \leq x \leq 14$). In agreement with prior simulations, the $B_6A_4B_6$ amphiphile with symmetric hydrocarbon blocks preferentially self-assembles into hexagonally perforated lamellae, whereas those with asymmetric hydrocarbon segments and $n \leq 12$ can form stable double gyroid networks. Within these double gyroid morphologies, interconnected channel domains are composed of sugar-based segments embedded in a continuous hydrocarbon matrix. Remarkably small feature sizes ranging from 1.92 to 2.26 nm are observed as the sugar volume fraction (f_A) varies from 0.23 to 0.29. Structural analyses further reveal distinct local enhancements in oxygen density—indicative of concentrated sugar-based segments—predominantly at the gyroid nodes, accompanied by reduced densities along the connecting struts. Additionally, a mean curvature analysis confirms that these fairly stiff oligomers form gyroid structures containing a higher fraction of regions with high curvature compared to idealized gyroid structures. Together with investigations of related miktoarm triblock oligomers ($A_oB_pB_q$), this study highlights the role of asymmetry in the molecular design of amphiphilic block oligomers, which facilitates the stabilization of network morphologies with ultra-small feature sizes and provides insight into the microscopic packing behavior of amphiphiles.

Received 30th January 2026,
Accepted 20th April 2026

DOI: 10.1039/d6lf00030d

rsc.li/RSCApplInter

1 Introduction

Block polymers and amphiphilic oligomers have emerged as versatile materials for applications as mesoporous materials and templates for inorganic analogs,^{1–3} thermoplastic elastomers,^{4,5} and drug delivery systems.^{6,7} Microphase separated linear block copolymers typically display domain spacings in the 10–50 nm range; however, high- χ (low- N) block oligomers—characterized by their small molecular size—can generate morphologies with feature dimensions below 5 nm,^{8–13} opening up new possibilities for nanofiltration, nanopatterning, and other nanoscale technologies.^{14–18}

Self-assembly in block polymer and amphiphilic oligomer systems yields a diverse array of ordered structures, including hexagonally perforated lamellae (HPL), hexagonally packed

cylinders (CYL), body-centered cubic micelles (BCC), and network (NET) morphologies.^{19–22} NET structures, characterized by bicontinuous interpenetrating domains,²³ are especially attractive for applications such as nanoporous membranes,^{24–26} energy storage devices,^{27–30} biophotonic constructs^{31,32} and photonic crystals.^{33–35} However, the stabilization of NET morphologies is hampered by packing frustration that restricts their formation to narrow compositional windows,^{36–38} and by the challenge of designing molecular architectures that can accommodate the varying curvatures inherent in these structures. For instance, the double gyroid (DG) phase exhibits pronounced variations in mean curvature across different local regions of the unit cell,³⁹ necessitating tailored molecular designs. Strategies to broaden the stability window of NET structures include blending components that naturally favor different morphologies¹¹ and developing innovative architectures such as coil-brush or bottlebrush polymers and shape-specific bolapolyphiles.^{40–46}

The drive for miniaturization further underscores the importance of achieving NET structures with ultra-small features. Melt-ordered block polymers are limited by their long chain lengths (N), which restrict the attainable pore sizes and unit cell dimensions in NET morphologies. To

^a Department of Chemical Engineering and Materials Science, University of Minnesota, 421 Washington Avenue SE, Minneapolis, Minnesota 55455-0132, USA. E-mail: lodge@umn.edu, siepmann@umn.edu

^b Chemical Theory Center, University of Minnesota, 207 Pleasant Street SE, Minneapolis, Minnesota 55455-0431, USA

^c Department of Chemistry, University of Minnesota, 207 Pleasant Street SE, Minneapolis, Minnesota 55455-0431, USA



overcome these constraints, recent efforts have focused on employing blocks with larger effective segmental interaction parameters (χ), enabling the stabilization of NET phases in low- N systems.⁴⁷ In this context, amphiphiles—with a large χ between hydrophilic and hydrophobic segments and their low molecular weight—are particularly effective at stabilizing NET structures with extremely small dimensions.^{48–52}

Our previous work, involving molecular simulations, synthesis of high-purity compounds, and experiments, has shown that amphiphilic block oligomers containing sugar-based (in either open or ring forms) and nonpolar hydrocarbon segments can form mesophases with remarkably small domain sizes.^{8–13} For instance, Shen *et al.* demonstrated that triblock amphiphiles, such as $B_6A_4B_6$, can form stable HPL with characteristic length scales approaching 1 nm,¹⁰ and Li *et al.* found that miktoarm triblock oligomers with two tails of different length can stabilize double gyroid NET structures.¹² Furthermore, self-consistent field theory (SCFT) studies on asymmetric ABA triblock copolymer melts indicate that introducing molecular asymmetry can stabilize DG structures, suggesting that rigid amphiphilic oligomers with similar triblock architectures may exhibit comparable scale-invariant phase behavior.⁵³

In the present study, molecular dynamics (MD) simulations employing molecular mechanics force fields are used to investigate the self-assembly of neat amphiphilic block oligomers into various morphologies. An asymmetric molecular design converts HPL-forming $B_6A_4B_6$ amphiphiles into $B_6A_4B_x$, which comprise a hydrophilic tetraol segment (A_4 , consisting of four $-CHOH-$ repeat units) and two hydrophobic alkyl segments (B_6 and B_x), each built from $-CH_2-$ repeat units (see Fig. 1). Moreover, the microscopic packing of amphiphiles in DG phases is analyzed using methods based on coordinates, density, clustering, and curvature projections, and the order-disorder transition is examined by tracking clustering and level surface distributions along the simulation trajectories.

These simulations are motivated by the possibility of accessing these asymmetric $B_6A_4B_x$ amphiphiles by an analogous approach to that reported by Barrreda *et al.* for $B_{13}A_6$ amphiphiles⁹ and extended by Mattson *et al.* to related diblock amphiphiles.⁵⁴ Specifically, tin-mediated allylation of erythrose (or another aldose) followed by olefin cross-metathesis with 1-pentene and tandem hydrogenation of the resulting would yield the B_6A_4 diblock oligomer. Selective oxidation of the terminal $-CH_2OH$ of the A_4 segment would yield an aldehyde, which could again undergo tin-mediated allylation, olefin cross metathesis, and hydrogenation to yield the desired $B_6A_4B_x$ ($x \geq 6$) amphiphile. The thermotropic liquid crystalline network morphologies adopted by these amphiphiles could then be

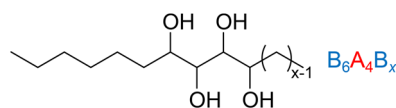


Fig. 1 Chemical structures of $B_6A_4B_x$ amphiphiles.

identified by small-angle X-ray scattering (SAXS), and they would be expected to exhibit no optical birefringence.⁹ While these synthesis and characterization experiments are in principle straightforward, optimization of the synthesis and purification to access useful quantities of these amphiphiles for complete molecular and supramolecular assembly characterization could be nontrivial. Thus, this motivates simulation studies of their expected properties prior to embarking on this potentially arduous synthesis task.

2 Methods

2.1 Molecular models and simulation details

The $B_6A_4B_x$ amphiphiles are modeled using the transferable potentials for phase equilibria united-atom (TraPPE-UA) force field.^{55–58} Detailed force field parameters are provided in the SI (see Tables S1 and S2). MD simulations are performed in the isobaric–isothermal (NPT) ensemble using GROMACS 2021.3.^{59,60} System sizes range from 1000 to 2000 molecules. Temperature and pressure are controlled *via* the Nosé–Hoover thermostat^{61,62} (with a time constant $\tau_T = 0.4$ ps) and the Parrinello–Rahman barostat⁶³ (with $\tau_p = 2$ ps), respectively. Electrostatic interactions are computed using the particle-mesh Ewald method,⁶⁴ and the p-LINCS algorithm is used to constrain O–H bond lengths,⁶⁵ which allows for a 2 fs integration time step. Initial disordered configurations are generated by short Monte Carlo (MC) simulations using coupled-decoupled configurational-bias (CD-CB) MC moves⁵⁶ in the canonical ensemble at a very high temperature of $T = 3000$ K (but harmonic bonds cannot break). Because the united-atom model utilizes CH pseudo-atoms also for the sugar-based block and the CD-CB regrowth algorithm does not preserve tacticity, each amphiphile should be viewed as a random mixture of stereoisomers. Systems are then equilibrated at $T = 445$ K and 1 bar using MD trajectories of at least 1 μ s, where equilibration is assessed through system energy and volume reaching converged values and analysis of static structure factors performed for 100 ns segments not showing any significant changes. Equilibration is followed by additional trajectories of 200 ns for HPL and 400 ns for DG phases used for detailed structural analyses. Comparisons between experimental and simulated phase boundaries and static structure factors for related A_6B_{13} diblock amphiphiles⁹ and $A_2B_xA_2$ ($8 \leq x \leq 12$) triblock amphiphiles¹⁰ and for the vapor–liquid equilibria of binary (methanol or ethanol)/ n -hexane mixtures⁵⁷ indicate that the non-polarizable TraPPE-UA force field yields very good predictions for the domain spacing of lamellar phases but overpredicts the effective χ value and, hence, phase transitions occur at higher temperatures than for the corresponding experimental systems. Visualization of simulation snapshots, including those showing dividing surfaces and ball-and-stick representations, is performed using Ovito and VMD.^{66–68}

2.2 System size tuning and workflow

Initial simulations for all $B_6A_4B_x$ systems are conducted in orthorhombic cells containing either 1000 or 2000 molecules.



This setup permits independent fluctuations in the x -, y -, and z -dimensions, thereby mitigating the effects of incommensurability,^{69,70} and is well-suited for morphologies with one- or two-dimensional periodicity (e.g., LAM and CYL structures), where domain spacing can be adjusted *via* rotations and lateral expansions or contractions perpendicular to the lamellar planes or cylinder axes. In contrast, for three-dimensional periodic morphologies (e.g., BCC and NET structures), 1000-molecule systems tend to yield locally segregated but globally disordered micelles or networks due to persistent incommensurability, unless the simulation box dimensions are integer multiples of the unit cell. To achieve ordered NET structures, it is critical to determine both the lattice parameter (a) and the number of molecules per unit cell (N_{UC}) in order to avoid distorted, metastable configurations.^{71–73} The unit cell dimension is estimated by calculating the structure factor $S(q)$ for disordered NET-like structures and identifying the broad peak position *via* the relation $a = 2\pi m/q^*$, where m corresponds to the first observable reflection spacing ratio for the morphology (e.g., $m = \sqrt{6}$ for DG). The value of N_{UC} is then estimated based on the average molecular volume derived from the initial simulations. It should be noted that the broad peak found in the disordered NET-like structures leads to considerable uncertainty in the estimation of a and, in some cases, it is advantageous to explore a range of N_{UC} values. For each $B_6A_xB_x$ system that initially forms disordered NET structures, simulations are restarted with $8N_{\text{UC}}$ molecules in a cubic box of length $L_{\text{box}} = 2a$, which facilitates the formation of ordered NET phases, such as double gyroid (DG), double diamond (DD), single gyroid (SG), and double primitive (DP, also known as plumber's nightmare). To promote ordering, a workflow for 3D NET simulations is employed that includes the application of a guiding field, generated by Gaussian interaction sites with varying strengths for polar and nonpolar beads and distributed within the minority and majority domains, respectively, of the candidate NET structures.^{11–13} After removal of the guiding field, the stability of each candidate NET morphology is assessed over a 1 μs trajectory in the NPT ensemble but maintaining a cubic box shape. The values of N and additional details regarding the DG unit cells are provided in Table 1.

In principle, it would be desirable to estimate the molar free energy for the different NET phases and for different system sizes. Here, we find that only one NET phase remains stable over these long trajectories, so this phase is certainly lower in free energy. However, simulations with slightly different N for the desired NET phase can yield stable trajectories. Since the systems differ in N , one cannot construct a reversible path from one size to another and instead would have to perform thermodynamic integration along a reversible path to the ideal-gas state at a common reference density. Given the complexity of the amphiphiles with inter- and intramolecular hydrogen bonding and a large number of torsional degrees of freedom, such a thermodynamic integration would encounter significant sampling problems and likely not allow for small enough uncertainties to determine which system size corresponds to

Table 1 Simulation parameters and data for $B_6A_xB_x$ ($6 \leq x \leq 14$) amphiphiles: number of molecules N in the simulation box (which for the DG morphology contains 8 unit cells), average molecular volume V_m , estimated volume fraction of polar segment f_A , morphology, and average domain spacing d^a

Compound	N	V_m [nm^3]	f_A	Morphology	d [nm]
$B_6A_4B_6$	1504	0.53	0.30	HPL	1.92
$B_6A_4B_7$	1448	0.56	0.28	DG	1.92
$B_6A_4B_8$	1448	0.59	0.27	DG	1.95
$B_6A_4B_9$	1640	0.63	0.25	DG	2.04
$B_6A_4B_{10}$	1766	0.66	0.24	DG	2.15
$B_6A_4B_{11}$	1872	0.69	0.23	DG	2.22
$B_6A_4B_{12}$	1872	0.72	0.22	DG	2.26
$B_6A_4B_{13}$	2000	0.75	0.21	DIS	2.39
$B_6A_4B_{14}$	2000	0.78	0.20	DIS	2.44

^a The statistical error for d ranges from 0.020 to 0.034 nm, in terms of the 95% confidence interval estimated by dividing the simulation trajectories into 10 blocks. However, the uncertainty for d introduced due to selecting a specific value of N is estimated to be about 0.05 nm.

the free energy minimum. It is reasonable to expect that the optimal value of N should increase with x for the $B_6A_xB_x$ amphiphiles, and the fact that $N = 1448$ is used for $B_6A_4B_7$ and $B_6A_4B_8$ (and $N = 1872$ is used for $B_6A_4B_{11}$ and $B_6A_4B_{12}$) indicates that the robust stability of the equilibrium state allows it to tolerate a certain degree of incommensurability, thereby not requiring the optimal number of molecules in the simulation box.⁶⁹ Consequently, although the most stable ordered structure is obtained after completion of the workflow, the system size may not be ideal. However, when the incommensurability is large, then the resulting stable NET structure exhibits structural imperfections. For $B_6A_4B_9$, $N = 1448$, 1544, and 1640 were explored and found to give d_{211} values of 1.98, 2.01, and 2.04 nm, respectively. Among these, $N = 1640$ yields a static structure factor with the minor peaks more clearly resolved (see Fig. S1), and its d_{211} value falls closer to the midway point between the d_{211} spacings for $B_6A_4B_8$ and $B_6A_4B_{10}$, thereby indicating that $N = 1640$ is the better choice among these three candidates.

3 Results and discussion

3.1 Phase behaviors of asymmetric $B_6A_xB_x$

As incrementing x increases the tail length by one CH_2 unit at a time, the molecular volume of the $B_6A_xB_x$ amphiphiles increases linearly (see Table 1 and Fig. S2). A linear regression analysis indicates that the incremental volume of the B_6A_4 segment is approximately 0.34 nm^3 and that of the B_6 segment is about 0.19 nm^3 . Consequently, the volume fraction of the hydrophilic segment (f_A) is estimated to vary from 0.30 (for $x = 6$) to 0.20 (for $x = 14$) (see Fig. S2).

For $x = 6$ (i.e., $B_6A_4B_6$), stable hexagonally perforated lamellae (HPL) are observed (see Fig. 2b). The periodicity of these structures is confirmed *via* the static structure factor (detailed calculation procedures can be found in the SI). Although the temperature is higher by 5 K compared to previous simulations for $B_6A_4B_6$,¹⁰ the structure factor is nearly identical, exhibiting a primary peak along with a



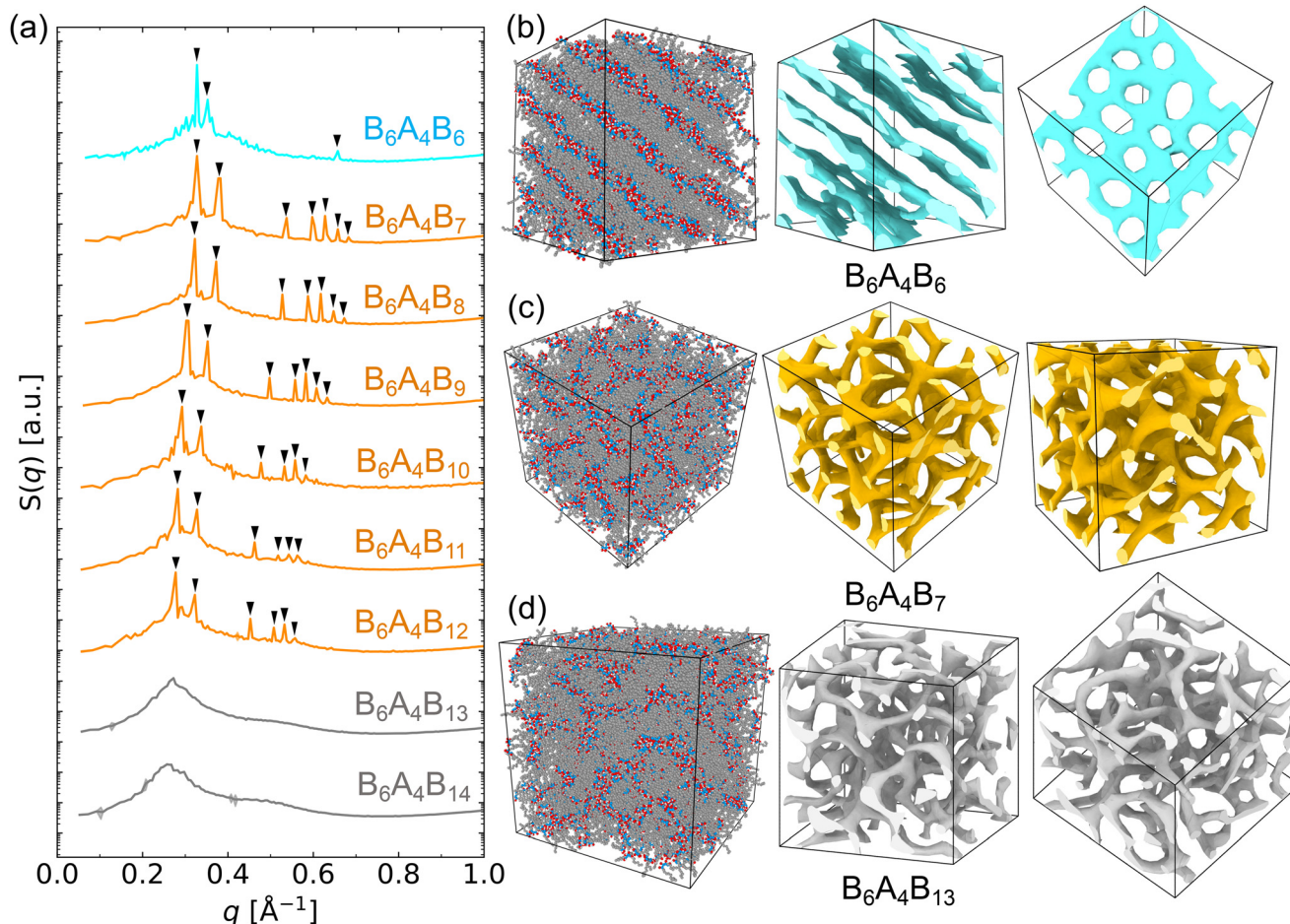


Fig. 2 (a) Static structure factors $S(q)$ of $B_6A_4B_x$ amphiphiles (with x ranging from 6 to 14). Molecular configuration snapshots in ball-and-stick representations (white and red spheres denote hydroxyl hydrogen and oxygen atoms, respectively; light blue and light gray spheres denote polar CH and non-polar (CH_2 or CH_3) pseudo-atoms, respectively), together with dividing surfaces between polar and nonpolar regions (shown from two different viewing angles), for the equilibrium morphologies of (b) $B_6A_4B_6$, (c) $B_6A_4B_7$ and (d) $B_6A_4B_{13}$.

closely spaced secondary peak that corresponds to the periodic arrangement of perforations in each layer (see Fig. 2a).

Stable double gyroid (DG) structures are observed for amphiphiles with x ranging from 7 to 12, with d_{211} -spacings increasing from 1.92 nm in $B_6A_4B_7$ to 2.26 nm in $B_6A_4B_{12}$ (see Fig. 2 and Table 1). The characteristic relative peak positions are located at 1 , $\sqrt{8/6}$, $\sqrt{16/6}$, $\sqrt{20/6}$, $\sqrt{22/6}$, $\sqrt{24/6}$, and $\sqrt{26/6}$, which are consistent with the $Ia\bar{3}d$ (Q^{230}) space group symmetry,⁷⁴ are detected in the structure factors. However, for $B_6A_4B_x$ with larger x values and closer to the order–disorder boundary anticipated based on linear triblock copolymers, low-intensity peaks at higher q become less discernible. To exclude alternative network structures and to verify that the equilibrium morphology of $B_6A_4B_x$ amphiphiles is indeed the DG phase, the workflow with guiding fields was also used to generate DD, SG, and DP structures, but these network structures are found to rapidly become disordered within 50 ns after removal of the guiding field (see Fig. S3 for the structural evolution of the $B_6A_4B_7$ system), thereby eliminating them as candidates for stable network structures and confirming that the DG

morphology represents the most stable state formed by self-assembly.

To further validate the quality of the DG structures formed by these amphiphilic oligomers, a level surface analysis is employed.^{75–79} The DG morphology is approximated by the level surface

$$\sin\left(2\pi\frac{x}{L}\right)\cos\left(2\pi\frac{y}{L}\right) + \sin\left(2\pi\frac{y}{L}\right)\cos\left(2\pi\frac{z}{L}\right) \cdots \cdots + \sin\left(2\pi\frac{z}{L}\right)\cos\left(2\pi\frac{x}{L}\right) = t \quad (1)$$

where x , y , and z denote the spatial coordinates, L is the unit cell size, and t is the level surface constant that determines the volume ratio between the gyroid channels and the matrix. Values satisfying $t > 1$ and $t < -1$ correspond to the right-handed and left-handed channels, respectively, and values satisfying $|t| \leq 1$ represent the matrix between the two channels. For the gyroid level surface, a critical t value of 1.413 is identified as the pinch-off surface, representing the threshold at which the gyroid channels are constricted at the struts.^{79,80} At this point, the channel volume is contributed almost entirely by the nodes, so that all points with $|t| \geq$



1.413 can be regarded as residing at the core of the gyroid nodes. To analyze the spatial distribution of molecules within the DG morphologies, the coordinates of all oxygen atoms in the simulation box are substituted into the level surface equation, and the resulting distribution of t is computed as a quality indicator. Fig. 3a displays the distribution curves of t values for DG morphologies formed by $B_6A_4B_x$ amphiphiles with x ranging from 7 to 12. For all six systems, two distinct and well-separated peaks are observed corresponding to the two gyroid channels which confirms that the molecules are accurately self-assembled into a DG structure with two clearly defined channel domains.

Complementarily, Fig. 3b presents a stacked bar chart that quantifies the proportion of t values inside versus outside the interval $[-1, 1]$. The histogram shows that less than 30% of the t values fall within this interval, indicating that the majority of oxygen atoms (and thus the A_4 segment of the amphiphiles) reside predominantly in the gyroid channels rather than in the interstitial matrix. This detailed analysis reinforces the conclusion that the DG morphology is the most stable equilibrium state. From Fig. 3b, the increasing

fraction of t values falling outside of the matrix interval indicates a higher concentration of oxygen atoms within the gyroid matrix. This trend suggests that the interfacial width between the channel and matrix domains is expanding, which constitutes a direct signature of the approach to the order–disorder transition.

For $B_6A_4B_x$ amphiphiles with larger x values (*i.e.*, $x = 13$ and 14), the molecules fail to self-assemble into CYL morphology or retain any of the NET morphologies and only a disordered phase (DIS) is observed after a comprehensive exploration of the workflow (see Fig. 2a). This occurs when the volume fraction of the hydrophilic segment (f_A) is approximately 0.21, a value that is close to the order–disorder boundary reported in previous SCFT studies on triblock polymers.⁵³ During the workflow exploration, various ordered phases were used as initial configurations for the MD simulations, including relatively stable hexagonally packed cylinders (CYL) and DG phases. When the initial configuration is CYL, $B_6A_4B_{13}$ maintains a relatively ordered structure with few defects for around 40 ns, whereas $B_6A_4B_{14}$ sustains order for only about 20 ns before transitioning to a DIS phase. Representative snapshots from the simulation trajectories are shown in Fig. S4. In the case of DG being set up as the initial configuration, the DG arrangement in the simulation of $B_6A_4B_{14}$ quickly vanishes, while $B_6A_4B_{13}$ fully transforms into a DIS phase after approximately 100 ns, but 3-fold connectors persist for a longer time (see Fig. S5). Moreover, static structure factors calculated separately over the 20–50, 50–100, 100–150, 900–1000, and 1900–2000 ns intervals clearly capture the DG-to-DIS transition for the $B_6A_4B_{13}$ and $B_6A_4B_{14}$ systems (see Fig. S6). For the $B_6A_4B_{13}$ system, the structure factor obtained from the 50–100 ns segment exhibits the first two characteristic DG peaks. Extended 2 μ s trajectories do not yield re-emergence of the DG morphology for the $B_6A_4B_{13}$ and $B_6A_4B_{14}$ systems.

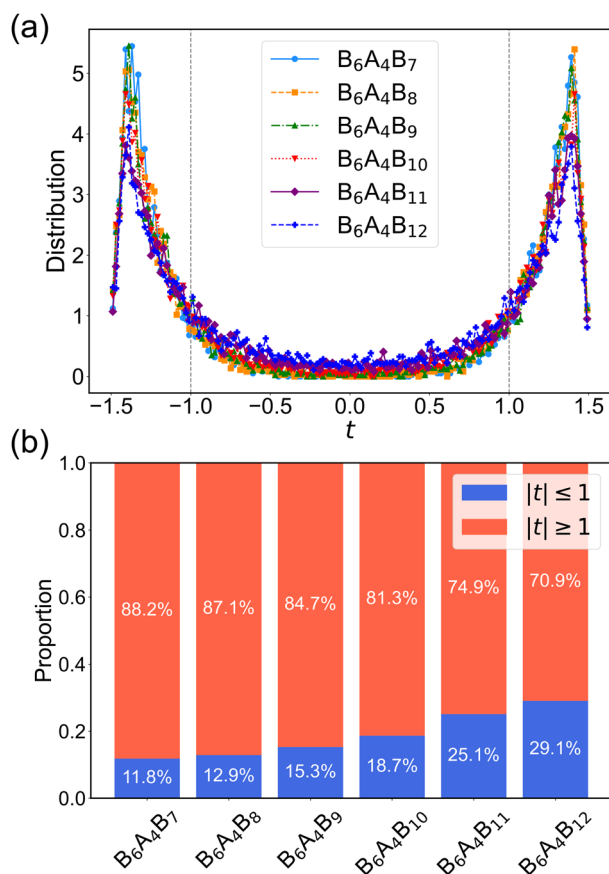


Fig. 3 (a) Level surface analysis of oxygen atom coordinates in DG-forming $B_6A_4B_x$ amphiphiles (with $x = 7$ – 12); gray dashed lines at $t = -1$ and $t = 1$ indicate approximate boundaries between the gyroid channels and the matrix. (b) Histogram of t values from the level surface analysis for oxygen atom coordinates with bars representing the proportion of values within and outside the $t \in [-1, 1]$ region.

3.2 Domain spacing, hydrogen bonding, and amphiphile packing

Stable DG structures are observed for amphiphiles with x ranging from 7 to 12, with d_{211} -spacings increasing from 1.92 nm in $B_6A_4B_7$ to 2.26 nm in $B_6A_4B_{12}$. While the increases in d_{211} values with addition of a methylene group vary from 0.03 to 0.11 nm, an unweighted linear fit yields a correlation coefficient of 0.988 and a slope of 0.075 ± 0.006 nm per CH_2 unit. Thus, the variation in step sizes may be caused by the specific system sizes used here not being always optimal.

As discussed in our prior work comparing the self-assembly of $A_2B_{12}A_2$ and $B_6A_4B_6$ triblock amphiphiles, the ability of the $B_6A_4B_6$ isomer to form intramolecular hydrogen bonds (HB) leads to a preference for U-shaped conformations and a stable HPL phase, whereas the $A_2B_{12}A_2$ isomer prefers more stretched conformations that bridge between two polar regions of a LAM structure.¹⁰ Here, we focus on the formation of intermolecular HBs in the $B_6A_4B_x$ amphiphiles as x is increased from 6 to 14 and the morphology changes from HPL to DG to DIS. The oxygen–oxygen radial distribution functions



(RDFs) for these systems are shown in Fig. 4(a). Given the low volume fraction of the polar block, f_A (see Table 1), the first peak in the OO RDF at 0.28 nm is very pronounced, followed by a broad second peak and a slow decay to a value near unity at 1.0 nm which reflects the cross-sectional size of the polar region. The heights of the first and second peaks decrease monotonically as x decreases. The decrease in peak heights does not indicate a decrease in hydrogen bonding, but reflects the increase in f_A which enters into the normalization of the RDFs. The number of HBs per molecules (see Fig. 4(b)) is obtained using an O–O distance less than 0.35 nm and an O–H···O angle greater than 150° as the HB criterion. Overall, it is clear that the number of HBs decreases as x increases (*i.e.*, the opposite trend as the peak heights in the RDFs) from a value of 4.78 for $B_6A_4B_6$ to 4.62 for $B_6A_4B_{14}$. The HB data also point to a discontinuous step as the morphology changes from HPL to DG. The statistical uncertainties are too large to conclude that the HB numbers decrease with increasing x for the DG-forming amphiphiles (and the slope would only be ≈ -0.01 HB per methylene unit). It should also be noted that, in the case that the optimal N_{UC} could be found for each amphiphile, a more systematic trend may emerge. On the other hand, there does not appear a discontinuous step as the morphology changes from DG to DIS.

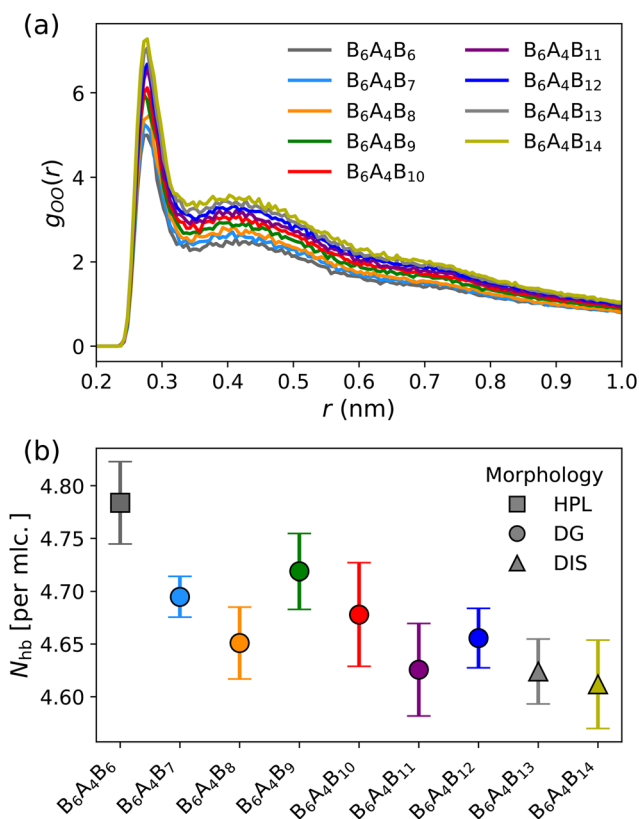


Fig. 4 (a) Intermolecular oxygen–oxygen radial distribution functions and (b) hydrogen bond numbers per molecule for the $B_6A_4B_x$ amphiphiles. The error bars reflect the 95% confidence interval estimated by dividing the trajectory into 10 blocks.

A three-dimensional analysis of the DG structures formed by $B_6A_4B_x$ amphiphiles is needed to elucidate microscopic phenomena in amphiphile packing. Because the hydrophilic A_4 segments assemble into gyroid channels, a Gaussian kernel density estimation (KDE) is applied to the oxygen atom coordinates of the A_4 segments for DG phases.^{81,82} The discrete atomic positions are transformed into a continuous probability density function, denoted by $\hat{f}(\mathbf{r})$, which represents the estimated probability density of finding an oxygen atom at a given point \mathbf{r} in space. A Gaussian kernel is employed, with each atom contributing according to

$$\hat{f}(\mathbf{r}) = \frac{1}{N_o} \sum_{i=1}^{N_o} \frac{1}{h^3 (2\pi)^{3/2}} \exp\left(-\frac{\|\mathbf{r}-\mathbf{r}_i\|^2}{2h^2}\right) \quad (2)$$

Here, N_o denotes the total number of oxygen atoms, and \mathbf{r}_i represents the coordinate of the i th atom. The bandwidth parameter h is set to 0.2, controlling the degree of smoothing applied to the density estimate.

For the DG morphology formed by $B_6A_4B_7$, the KDE is visualized in three-dimensional space (see Fig. 5a), where each point corresponds to an oxygen atom and the color indicates the normalized density (ranging from 0 to 1). It is observed that isolated points exhibit lower density, whereas points located within the gyroid channels display higher density. To better highlight these high-density regions, Fig. S7 marks all points with density values above the 95th percentile (*i.e.*, 0.87) with red circles. These highlighted points are predominantly situated near the gyroid nodes rather than the struts, indicating that a tighter packing of the hydrophilic A_4 segments is required at the nodes to stabilize the DG structure.

To quantitatively analyze the spatial distribution of these points, the gyroid level surface (see eqn (1)) serves as an effective mathematical tool to examine the distribution of the level surface constant t derived from the oxygen atom coordinates. Fig. S8 presents a scatter plot of $|t|$ values versus their KDE density, which clearly shows that high KDE values are only found for $|t| > 1$. In addition, the frequency histograms along the top and left margins of Fig. S8 reveal that most points are located in the region where $|t| \geq 1.2$, with the high-density points concentrated near $|t| = 1.3$, *i.e.*, close to the center of the nodes.

For DG structures, the right-handed and left-handed gyroid channels each comprise eight nodes, resulting in a total of 16 nodes per unit cell. By calculating the average density of oxygen atoms as a function of the distance from these nodes, the presence of local oxygen density enhancement can be evaluated. Taking the coordinates of the nodes as the centers of spheres with a cutoff radius r_{cut} (with the nearest-neighbor distance between nodes defined as d_{cut}), the average density of oxygen atoms within spherical shells (for increasing r_{cut} bins) is computed to obtain a density versus r_{cut}/d_{cut} curve. The resulting curve is shown in Fig. 5b, which represents an average over DG-forming $B_6A_4B_x$ amphiphiles with $x = 7$ to 12; more detailed curves for each



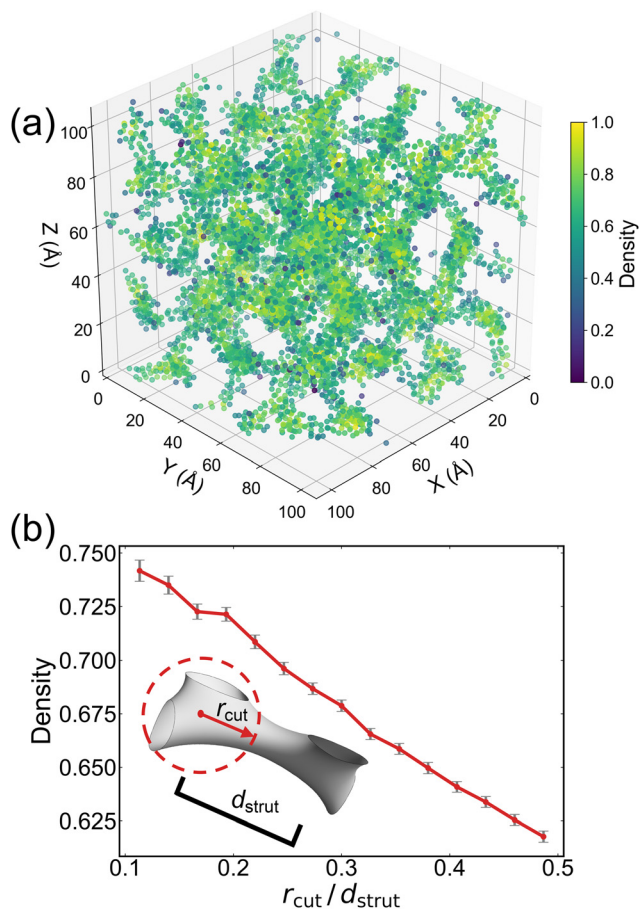


Fig. 5 (a) Normalized density of oxygen atom coordinates obtained via three-dimensional kernel density estimation for $B_6A_4B_{10}$. (b) Normalized density of oxygen atom coordinates as a function of cutoff distance, averaged over DG-forming $B_6A_4B_x$ amphiphiles (with $x = 7$ – 12); error bars represent the standard error of the mean. Inset: Schematic definition of r_{cut} and d_{strut} on the gyroid dividing surface.

individual DG-forming amphiphile are provided in Fig. S9. Because the density is calculated as an average over all points within each spherical shell, the number of points in the shell does not affect the result. Moreover, as most oxygen atoms are located in the gyroid channels (as demonstrated in Fig. 3a), increasing r_{cut} results in the shell comprising progressively more points from the struts, with almost no contribution from the gyroid matrix. Fig. 5b shows a pronounced decrease in density, confirming that the nodes indeed exhibit a higher concentration of oxygen atoms and, consequently, require a greater number of hydrophilic A_4 segments for assembly.

3.3 Clustering analysis and order–disorder phase transition

One of the most prominent features of the DG structure is the presence of two interwoven, segregated gyroid channels with opposite chirality.⁸³ Although many visualization methods—such as 2D/3D TEM or software tools like VMD—are available in experiments and simulations, it remains challenging to

automatically differentiate the two channels on a microscopic level. To more definitively identify the existence of two segregated clusters within the simulation box, density-based spatial clustering of applications with noise (DBSCAN)⁸⁴ is applied to the oxygen atom coordinates extracted from the DG phase simulations. In DBSCAN, a point is classified as a core point if the number of neighboring points within a radius (ϵ) is greater than or equal to a specified minimum (min_samples). To account for periodic boundary conditions, the oxygen atom coordinates are first expanded by replicating the simulation box in all spatial directions. DBSCAN is then executed with $\epsilon = 5.0$ Å and min_samples = 5, such that regions of high oxygen density are automatically identified while points that do not meet the criteria are classified as noise. We find that box replication is essential to avoid oxygen atoms near the faces, edges, and corners being misclassified as belonging to separate clusters (see Fig. S10). While there is less sensitivity to the choice of ϵ , using a value of 4.0 Å (*i.e.*, less than the position of the second minimum in the O–O RDF, see Fig. 4) leads to significantly more noise in the DBSCAN analysis and using a very large value would lead to only a single cluster being detected.

The DBSCAN analysis for the $B_6A_4B_8$ system indicates two main clusters that correspond to the two interwoven gyroid channels (see Fig. 6a). To further verify that the two major clusters correspond to gyroid channels with opposite chirality, a level surface analysis is performed. Fig. 6b clearly shows that the oxygen atom coordinates in the orange and blue clusters from Fig. 6a are predominantly located in regions where $t > 1$ (the right-handed channel) and $t < -1$ (the left-handed channel), respectively. This indicates that DBSCAN successfully identifies two segregated clusters, with almost no distribution in the region $|t| < 1$ corresponding to the gyroid matrix, which is mostly occupied by CH_2/CH_3 groups. Moreover, statistical analysis of the number of points in the DBSCAN clusters reveals that the two major clusters (orange and blue) contain approximately equal numbers of points and significantly more than any other cluster or the noise. Moreover, slices taken along the (111), (110), and (211) directions of the DBSCAN clustering results demonstrate that the internal DG structure is well preserved (Fig. 6c).

In the workflow exploring possible equilibrium morphologies for $B_6A_4B_x$ amphiphiles, a frequently observed order–disorder phase transition—from the initial structure to a disordered (DIS) state—is of particular interest, especially the transition from the DG structure to a DIS structure. Based on the workflow, the preferred periodicity of the amphiphiles is first determined by MD simulations *via* the primary peak position q^* in the static structure factor. This enables the system size of the different morphologies to be approximately commensurate with the preferred lattice periodicity and, as a result, the primary peak in the structure factor does not shift significantly during the order–disorder transition (see Fig. S6). However, snapshots of the taken after the transition occurred reveal the prevalence of 3-fold connectors in the bicontinuous DIS structures (see Fig. S3–S5).



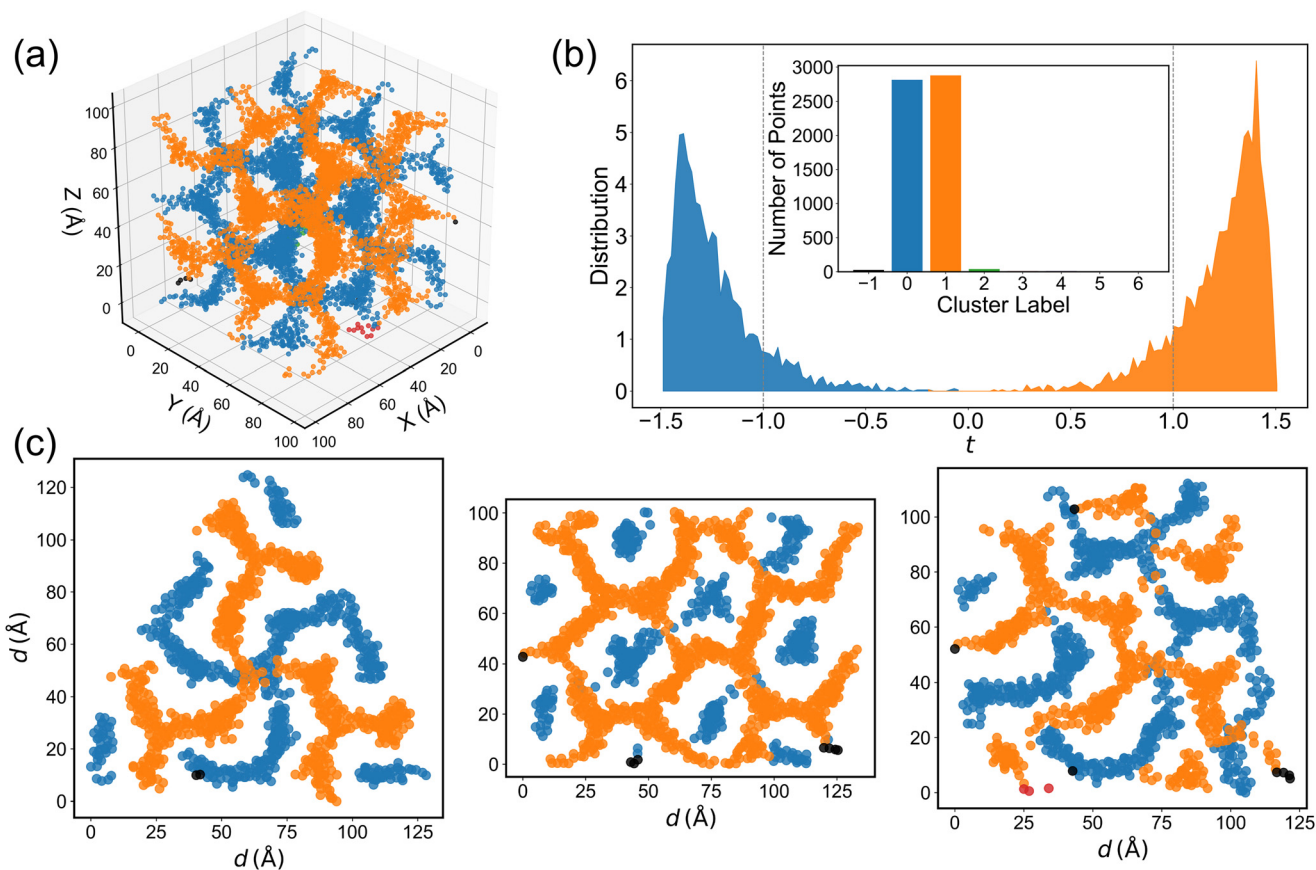


Fig. 6 (a) DBSCAN clustering analysis of oxygen atom coordinates in the equilibrium morphology of $B_6A_4B_8$. Oxygen atoms belonging to the two distinct clusters are shown in blue and orange, while noise points are rendered in black. (b) Level surface analysis of oxygen atom coordinates for the two major clusters identified by DBSCAN; inset: number of data points per cluster (where noise points are grouped at cluster index -1). (c) Sliced views of DBSCAN clustering results along the (111), (110), and (211) planes, each with a 20 Å thickness, from the equilibrated DG structure of $B_6A_4B_8$ after 1 μ s MD simulation.

Consequently, DBSCAN is employed to investigate whether multiple locally segregated clusters can form within these DIS structures. Fig. 7a displays the DBSCAN analysis results for the $B_6A_4B_8$ system, which was initially guided into a DG structure, over a 1 μ s MD simulation trajectory with clustering analysis performed every 10 ns. It is observed that, along the simulation trajectory, the initially guided nearly 1:1 segregation of the two gyroid channels is quickly lost but reappears near 350 ns. This suggests that, at the microscopic scale, a “bridge” forms between the two initially segregated gyroid channels, leading to them merging into one cluster and preventing DBSCAN from clearly differentiating the two channels. As the simulation progresses beyond 350 ns the system re-stabilizes into an arrangement containing two clusters in an almost 1:1 ratio, but transient occurrences of a dominant cluster caused by bridging defects are still observed. The frequency of these defects appears to decrease over time, with considerably fewer defect-containing snapshots in the 700–1000 ns interval compared to earlier intervals.

For the $B_6A_4B_{13}$ amphiphile, which transitions to a DIS structure, the situation is markedly different. Fig. 7b shows the evolution of the proportions of the two largest clusters from the DBSCAN analysis when the initial configuration is

DG. Here, only the first 100 ns of the trajectory are considered with DBSCAN clustering performed at 1 ns intervals. During the first 25 ns, the guided DG structure is barely maintained; although some frames exhibit instances of two clusters with intermittent connections, the balance between the two clusters is rapidly lost as the simulation progresses. After 25 ns, a single dominant cluster persists throughout indicating a bicontinuous structure. This observation is consistent with the DIS snapshot shown in Fig. S5. Notably, the static structure factors calculated over the 20–50 ns interval still display distinct DG peaks (see Fig. S6), implying that despite the local absence of two segregated gyroid channels, the spatial arrangement of $B_6A_4B_{13}$ amphiphiles retains some periodic characteristics of the DG structure. This observation is corroborated by the level surface analysis (see Fig. 7c), which shows that, at 20 ns, most oxygen atom coordinates remain in regions with $|t| > 1$ (indicative of the gyroid channels). Although the two peaks corresponding to the regions $t > 1$ and $t < -1$ gradually diminish over time, the system still exhibits certain DG features even at 80 ns, with the A_4 segments predominantly located within the gyroid channels.

These results suggest that the level surface analysis lags behind both the DBSCAN clustering and the static structure



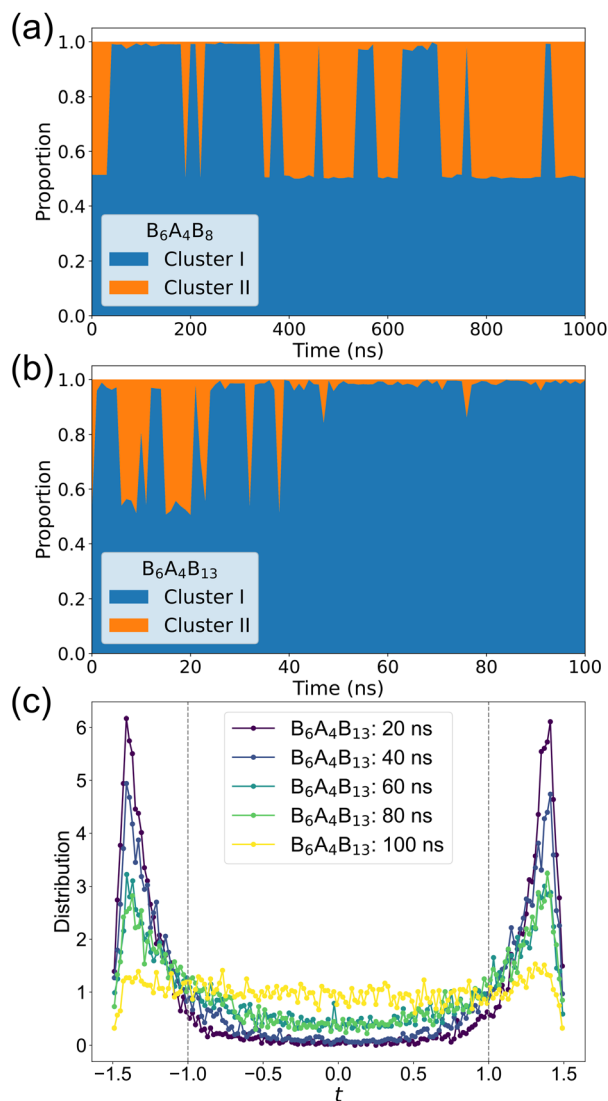


Fig. 7 DBSCAN clustering analysis for simulation trajectories initiated from the DG phase: (a) $B_6A_4B_8$ forming a stable DG phase (1 μ s trajectory, sampled every 10 ns) and (b) $B_6A_4B_{13}$ transitioning into a bicontinuous DIS phase (100 ns trajectory, sampled every 1 ns). Clusters I and II represent the largest and second largest clusters, respectively. (c) Level surface analysis of oxygen atom coordinates in $B_6A_4B_{13}$ amphiphiles at selected simulation snapshots taken at 20, 40, 60, 80, and 100 ns.

factor analysis. During the DG–DIS transition, defects such as inter-channel “bridges” form first, resulting in the merging of the two gyroid channels at a local scale (as detected by DBSCAN). Subsequently, the DG periodicity is gradually disrupted at larger scales, and finally, the initially guided A_4 segments begin to diffuse into other regions of the simulation box. These phenomena are captured sequentially by DBSCAN clustering, static structure factor calculations, and level surface analysis, respectively.

3.4 Mean curvature analysis

The mean curvature H is an effective approach to explore the dividing surfaces within a DG structure.^{36,39} Fig. 8a presents a

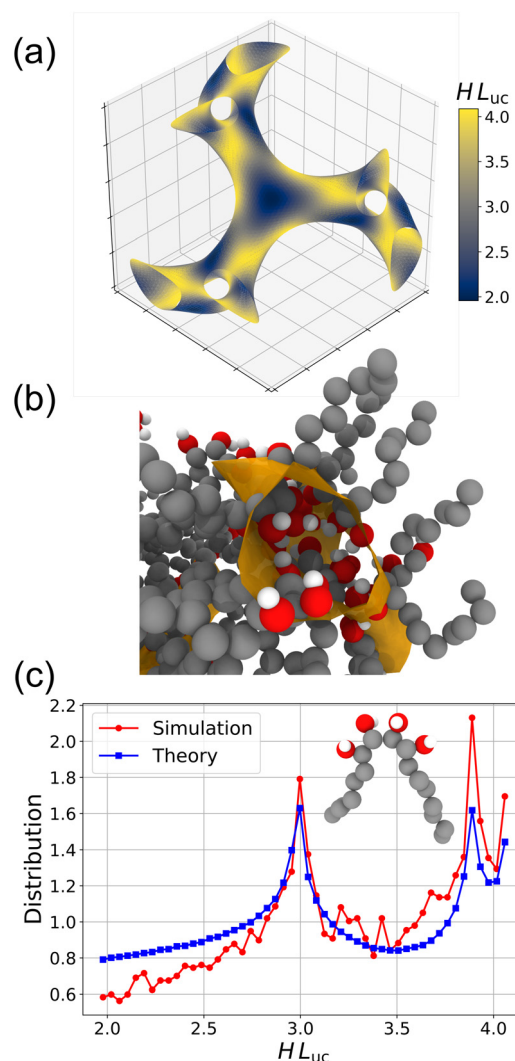


Fig. 8 (a) Dimensionless mean curvature, HL_{uc} , obtained by multiplying the mean curvature H by the unit cell parameter, L_{uc} . The surface normal is defined so that H is always positive; the depicted gyroid level surface corresponds to $t = 1.1$. (b) Zoomed-in simulation snapshot of a gyroid node formed by $B_6A_4B_7$, with the interface between polar and nonpolar regions shown in orange. (c) Distribution of HL_{uc} evaluated at the centers of the second and third hydroxyl carbons of DG-forming $B_6A_4B_x$ amphiphiles ($x = 7-12$); inset shows a schematic representation of a $B_6A_4B_7$ amphiphile.

three-dimensional visualization of the gyroid level surface, obtained by solving the implicit gyroid level surface equation with the parameter $t = 1.1$. The iso-surface is extracted *via* the marching cubes algorithm.⁸⁵ The average mean curvature at each vertex is computed by evaluating the gyroid level surface equation (see eqn (1)) using analytically derived first and second order derivatives, and the mean curvature values, H , are rendered dimensionless by multiplying them by the unit cell parameter, L_{uc} . As shown in Fig. 8a, the complex topology of the gyroid structure is clearly depicted, highlighting both its geometric features and the local variations in HL_{uc} . Notably, the surface is relatively flat near the gyroid nodes—resulting in smaller values of $H L_{uc}$ —and more curved along the struts, where HL_{uc} is correspondingly larger.



At the microscopic level, the orientation of DG-forming $B_6A_4B_x$ amphiphiles on regions of differing curvature on the gyroid surface can be investigated. Fig. 8b shows a zoomed-in snapshot of a gyroid node from a DG structure formed by $B_6A_4B_7$. Since the dividing surface separates the hydrophilic A_4 segments from the hydrophobic B_x segments, the A_4 segments are expected to reside primarily within the dividing surface. As observed in the snapshot, the A_4 segments—connected at both ends to hydrophobic B_x segments—do not penetrate deeply into the exterior of the dividing surface. Accordingly, the centers of the second and third hydroxyl carbons are selected as representative markers for the positions of the amphiphiles near the dividing surface.

Fig. 8c presents the distribution of the dimensionless mean curvature HL_{uc} obtained from both simulation and theoretical analyses. For the simulation data, the coordinates of the centers of the second and third hydroxyl carbons are projected onto the implicit gyroid level surface with $|t| = 1.1$ using a Newton–Raphson scheme. The corresponding curvatures at these projection points are then computed, and the results are averaged over DG-forming $B_6A_4B_x$ amphiphiles with $x = 7$ to 12 to reduce the noise resulting from thermal fluctuations prevalent for the short amphiphiles and the relatively small system size. Individual curves for each DG-forming amphiphile are shown in Fig. S11. For the theoretical curve, the marching cubes algorithm is applied to extract the corresponding iso-surfaces, and the mean curvature at the mesh vertices is computed based on local differential geometry. An area-weighted average is subsequently determined for each triangle of the extracted surface, and the resulting data are normalized to yield a distribution. Using different $|t|$ values to define the surface does not qualitatively alter the shape of the curvature distributions but changes the HL_{uc} range and the relative heights for the two peaks (see Fig. S12). To further reduce noise in the simulation data, only the magnitude of the mean curvature is considered, disregarding its sign. It should be noted that, according to the conventional definition of the surface normal, the two channels should exhibit mean curvatures of opposite signs (as shown in Fig. S13). The comparison of these curves provides insight into the extent to which the local curvature statistics obtained from the simulation data generally conform to those predicted by the idealized gyroid level surface. Both curves display two distinct peaks found at the same two HL_{uc} values, and the overall shapes of the two curves match fairly well. However, the distribution obtained from the MD simulations exhibits an increasing trend for the baseline leading to a lower fraction of amphiphile molecules found in regions of lower values of HL_{uc} and a higher peak at $HL_{uc} \approx 3.9$ than at 3.0. This discrepancy arises because the stiff $B_6A_4B_x$ amphiphiles, which preferentially fold into V-shaped conformations,¹¹ respond to packing frustration caused by different regions of the gyroid dividing surface possessing different curvature. Near the gyroid nodes, the idealized surface is relatively flat with low curvature; however, the excluded volume of the

hydrophobic tails cannot be geometrically accommodated within the limited space of the matrix. In contrast, in the highly curved strut regions, the shape of the amphiphiles can be more easily accommodated.

4 Conclusion

MD simulations are employed to investigate the phase behavior of $B_6A_4B_x$ triblock amphiphilic oligomers, which consist of polar, sugar-based (A_4) segments and non-polar, hydrocarbon (B_6 and B_x) segments. $B_6A_4B_6$ amphiphiles self-assemble into HPL, while those with $x = 7$ to 12 form DG structures. In contrast, $B_6A_4B_{13}$ and $B_6A_4B_{14}$ do not attain stable ordered states, instead forming DIS phases. DG structures are stabilized across a range of A_4 volume fractions (f_A) from 0.22 to 0.28, with domain spacings varying from 1.92 nm to 2.26 nm. A Gaussian KDE analysis of the oxygen atom coordinates within DG morphologies reveals that the oxygen density is locally enhanced at the gyroid nodes and reduced along the struts. Furthermore, DBSCAN-based clustering accurately distinguishes the two gyroid channels of opposite chirality, which facilitates the detection of a bridging phenomenon during the DG-to-DIS transition. Mean curvature analysis demonstrates that regions with higher curvature are able to accommodate a higher fraction of amphiphile molecules compared to the surface fraction of idealized gyroid structures. This work demonstrates the value of asymmetric molecular design in stabilizing DG structures and provides insight into the microscopic packing behavior of amphiphiles.

Author contributions

Daoyuan Li – conceptualization; data curation; investigation; methodology; software; visualization; writing – original draft. Mahesh Mahanthappa – conceptualization; supervision; writing – review & editing. Timothy Lodge – conceptualization; supervision; writing – review & editing. Ilja Siepmann – conceptualization; methodology; supervision; writing – review & editing.

Conflicts of interest

There are no conflicts of interest to declare.

Data availability

The data supporting this article have been included as part of the supplementary information (SI).

Supplementary information: force field details, calculation of structure factors, tables with force field parameters and additional figures. See DOI: <https://doi.org/10.1039/d6lf00030d>.



Acknowledgements

This work was supported by the National Science Foundation through the University of Minnesota MRSEC under Award DMR-2011401. Computer resources were provided by this NSF award and by the Minnesota Supercomputing Institute.

References

- R. M. Dorin, H. Sai and U. Wiesner, *Chem. Mater.*, 2014, **26**, 339–347.
- L. Xiang, Q. Li, C. Li, Q. Yang, F. Xu and Y. Mai, *Adv. Mater.*, 2023, **35**, 2207684.
- D. Zhao, J. Feng, Q. Huo, N. Melosh, G. H. Fredrickson, B. F. Chmelka and G. D. Stucky, *Science*, 1998, **279**, 548–552.
- R. K. W. Spencer and M. W. Matsen, *Macromolecules*, 2017, **50**, 1681–1687.
- M. Steube, T. Johann, R. D. Barent, A. H. Mueller and H. Frey, *Prog. Polym. Sci.*, 2022, **124**, 101488.
- H. He, K. Rahimi, M. Zhong, A. Mourran, D. R. Luebke, H. B. Nulwala, M. Möller and K. Matyjaszewski, *Nat. Commun.*, 2017, **8**, 14057.
- S. Ha, Y. La and K. T. Kim, *Acc. Chem. Res.*, 2020, **53**, 620–631.
- Q. P. Chen, L. Barreda, L. E. Oquendo, M. A. Hillmyer, T. P. Lodge and J. I. Siepmann, *ACS Nano*, 2018, **12**, 4351–4361.
- L. Barreda, Z. Shen, Q. P. Chen, T. P. Lodge, J. I. Siepmann and M. A. Hillmyer, *Nano Lett.*, 2019, **19**, 4458–4462.
- Z. Shen, J. L. Chen, V. Vernadskaja, S. P. Ertem, M. K. Mahanthappa, M. A. Hillmyer, T. M. Reineke, T. P. Lodge and J. I. Siepmann, *J. Am. Chem. Soc.*, 2020, **142**, 9352–9362.
- Z. Shen, K. Luo, S. J. Park, D. Li, M. K. Mahanthappa, F. S. Bates, K. D. Dorfman, T. P. Lodge and J. I. Siepmann, *JACS Au*, 2022, **2**, 1405–1416.
- D. Li, Z. Shen, P. Chen, M. K. Mahanthappa, K. D. Dorfman, T. P. Lodge and J. I. Siepmann, *JACS Au*, 2025, **5**, 3387–3398.
- C. Zheng, K. Luo, S. Das, P. Chen, Z. Shen, J. Jaye, D. Li, M. A. Calabrese, T. M. Reineke and M. K. Mahanthappa, *et al.*, *J. Phys. Chem. B*, 2025, **129**, 8231–8243.
- J. Zhang, X. Yu, P. Yang, J. Peng, C. Luo, W. Huang and Y. Han, *Macromol. Rapid Commun.*, 2010, **31**, 591–608.
- S. Das, C. Zheng, T. P. Lodge, J. I. Siepmann, M. K. Mahanthappa, M. A. Calabrese and T. M. Reineke, *Biomacromolecules*, 2024, **25**, 1291–1302.
- S. P. Nunes, *Macromolecules*, 2016, **49**, 2905–2916.
- L. Qiao, D. A. Vega and F. Schmid, *Macromolecules*, 2024, **57**, 4629–4634.
- S. Maekawa, T. Seshimo, T. Dazai, K. Sato, K. Hatakeyama-Sato, Y. Nabaie and T. Hayakawa, *Nat. Commun.*, 2024, **15**, 5671.
- A. C. Finnefrock, R. Ulrich, G. E. S. Toombes, S. M. Gruner and U. Wiesner, *J. Am. Chem. Soc.*, 2003, **125**, 13084–13093.
- S. Cui, E. A. Murphy, S. Santra, F. S. Bates and T. P. Lodge, *ACS Nano*, 2025, **19**, 1211–1221.
- V. Abetz and P. F. W. Simon, *Advances in Polymer Science*, in *Block Copolymers*, ed. V. Abetz, Springer, 2005, vol. 189, pp. 125–212.
- S. Cui, B. Zhang, L. Shen, F. S. Bates and T. P. Lodge, *J. Am. Chem. Soc.*, 2022, **144**, 21719–21727.
- L. Han and S. Che, *Adv. Mater.*, 2018, **30**, 1705708.
- H. Uehara, T. Yoshida, M. Kakiage, T. Yamanobe, T. Komoto, K. Nomura, K. Nakajima and M. Matsuda, *Macromolecules*, 2006, **39**, 3971–3974.
- D. L. Gin, J. E. Bara, R. D. Noble and B. J. Elliott, *Macromol. Rapid Commun.*, 2008, **29**, 367–389.
- L. Li, L. Schulte, L. D. Clausen, K. M. Hansen, G. E. Jonsson and S. Ndoni, *ACS Nano*, 2011, **5**, 7754–7766.
- R. L. Kerr, S. A. Miller, R. K. Shoemaker, B. J. Elliott and D. L. Gin, *J. Am. Chem. Soc.*, 2009, **131**, 15972–15973.
- E. J. W. Crossland, M. Kamperman, M. Nedelcu, C. Ducati, U. Wiesner, D.-M. Smilgies, G. E. S. Toombes, M. A. Hillmyer, S. Ludwigs and U. Steiner, *et al.*, *Nano Lett.*, 2009, **9**, 2807–2812.
- E. J. W. Crossland, M. Nedelcu, C. Ducati, S. Ludwigs, M. A. Hillmyer, U. Steiner and H. J. Snaith, *Nano Lett.*, 2009, **9**, 2813–2819.
- M. C. Orilall and U. Wiesner, *Chem. Soc. Rev.*, 2011, **40**, 520–535.
- V. Saranathan, C. O. Osuji, S. G. J. Mochrie, H. Noh, S. Narayanan, A. Sandy, E. R. Dufresne and R. O. Prum, *Proc. Natl. Acad. Sci. U. S. A.*, 2010, **107**, 11676–11681.
- B. D. Wilts, K. Michielsen, H. De Raedt and D. G. Stavenga, *J. R. Soc., Interface*, 2012, **9**, 1609–1614.
- M. Maldovan, A. M. Urbas, N. Yufa, W. C. Carter and E. L. Thomas, *Phys. Rev. B: Condens. Matter Mater. Phys.*, 2002, **65**, 165123.
- M. Stefik, S. Guldin, S. Vignolini, U. Wiesner and U. Steiner, *Chem. Soc. Rev.*, 2015, **44**, 5076–5091.
- J. A. Dolan, B. D. Wilts, S. Vignolini, J. J. Baumberg, U. Steiner and T. D. Wilkinson, *Adv. Opt. Mater.*, 2015, **3**, 12–32.
- M. W. Matsen and F. S. Bates, *Macromolecules*, 1996, **29**, 7641–7644.
- S. Hyde, Z. Blum, T. Landh, S. Lidin, B. Ninham, S. Andersson and K. Larsson, *The Language of Shape: The Role of Curvature in Condensed Matter: Physics, Chemistry and Biology*, Elsevier, 1996.
- F. S. Bates and G. H. Fredrickson, *Phys. Today*, 1999, **52**, 32–38.
- M. W. Matsen, *J. Phys.: Condens. Matter*, 2001, **14**, R21.
- S. J. Park, G. K. Cheong, F. S. Bates and K. D. Dorfman, *Macromolecules*, 2021, **54**, 9063–9070.
- K. Kawamoto, M. Zhong, K. R. Gadelrab, L.-C. Cheng, C. A. Ross, A. Alexander-Katz and J. A. Johnson, *J. Am. Chem. Soc.*, 2016, **138**, 11501–11504.
- Y. Rokhlenko, K. Kawamoto, J. A. Johnson and C. O. Osuji, *Macromolecules*, 2018, **51**, 3680–3690.
- L. Jiang, D. Nykypanchuk, V. J. Pastore and J. Rzaevyev, *Macromolecules*, 2019, **52**, 8217–8226.
- S. Poppe, X. Cheng, C. Chen, X. Zeng, R.-b. Zhang, F. Liu, G. Ungar and C. Tschierske, *J. Am. Chem. Soc.*, 2020, **142**, 3296–3300.
- S. Poppe, C. Chen, F. Liu and C. Tschierske, *Chem. Commun.*, 2018, **54**, 11196–11199.



- 46 M. Poppe, C. Chen, H. Ebert, S. Poppe, M. Prehm, C. Kerzig, F. Liu and C. Tschierske, *Soft Matter*, 2017, **13**, 4381–4392.
- 47 C. Sinturel, F. S. Bates and M. A. Hillmyer, *ACS Macro Lett.*, 2015, **4**, 1044–1050.
- 48 S. R. Nowak, K. K. Lachmayr, K. G. Yager and L. R. Sita, *Angew. Chem., Int. Ed.*, 2021, **60**, 8710–8716.
- 49 C. Chen, R. Kieffer, H. Ebert, M. Prehm, R.-b. Zhang, X. Zeng, F. Liu, G. Ungar and C. Tschierske, *Angew. Chem., Int. Ed.*, 2020, **59**, 2725–2729.
- 50 X. Zeng, M. Prehm, G. Ungar, C. Tschierske and F. Liu, *Angew. Chem., Int. Ed.*, 2016, **55**, 8329–8332.
- 51 X. Zeng, S. Poppe, A. Lehmann, M. Prehm, C. Chen, F. Liu, H. Lu, G. Ungar and C. Tschierske, *Angew. Chem., Int. Ed.*, 2019, **58**, 7375–7378.
- 52 F. Liu, M. Prehm, X. Zeng, C. Tschierske and G. Ungar, *J. Am. Chem. Soc.*, 2014, **136**, 6846–6849.
- 53 M. W. Matsen, *J. Chem. Phys.*, 2000, **113**, 5539–5544.
- 54 I. Mattson, J. Majoinen, M. Lahtinen, T. Sandberg, A. Fogde, T. Saloranta-Simell, O. J. Rojas, O. Ikkala and R. Leino, *Soft Matter*, 2023, **19**, 8360–8377.
- 55 M. G. Martin and J. I. Siepmann, *J. Phys. Chem. B*, 1998, **102**, 2569–2577.
- 56 M. G. Martin and J. I. Siepmann, *J. Phys. Chem. B*, 1999, **103**, 4508–4517.
- 57 B. Chen, J. J. Potoff and J. I. Siepmann, *J. Phys. Chem. B*, 2001, **105**, 3093–3104.
- 58 J. M. Stubbs, J. J. Potoff and J. I. Siepmann, *J. Phys. Chem. B*, 2004, **108**, 17596–17605.
- 59 D. Van Der Spoel, E. Lindahl, B. Hess, G. Groenhof, A. E. Mark and H. J. Berendsen, *J. Comput. Chem.*, 2005, **26**, 1701–1718.
- 60 M. J. Abraham, T. Murtola, R. Schulz, S. Páll, J. C. Smith, B. Hess and E. Lindahl, *SoftwareX*, 2015, **1**, 19–25.
- 61 S. Nosé, *J. Chem. Phys.*, 1984, **81**, 511–519.
- 62 W. G. Hoover, *Phys. Rev. A: At., Mol., Opt. Phys.*, 1985, **31**, 1695–1697.
- 63 M. Parrinello and A. Rahman, *J. Appl. Phys.*, 1981, **52**, 7182–7190.
- 64 U. Essmann, L. Perera, M. L. Berkowitz, T. Darden, H. Lee and L. G. Pedersen, *J. Chem. Phys.*, 1995, **103**, 8577–8593.
- 65 B. Hess, H. Bekker, H. J. Berendsen and J. G. Fraaije, *J. Comput. Chem.*, 1997, **18**, 1463–1472.
- 66 A. Stukowski, *Modell. Simul. Mater. Sci. Eng.*, 2009, **18**, 015012.
- 67 A. Stukowski, *JOM*, 2014, **66**, 399–407.
- 68 W. Humphrey, A. Dalke and K. Schulten, *J. Mol. Graphics*, 1996, **14**, 33–38.
- 69 A. Arora, D. C. Morse, F. S. Bates and K. D. Dorfman, *Soft Matter*, 2015, **11**, 4862–4867.
- 70 J. Glaser, J. Qin, P. Medapuram and D. C. Morse, *Macromolecules*, 2014, **47**, 851–869.
- 71 T. Dotera, *Phys. Rev. Lett.*, 2002, **89**, 205502.
- 72 F. J. Martinez-Veracoechea and F. A. Escobedo, *J. Chem. Phys.*, 2006, **125**, 104907.
- 73 P. W. Schönhöfer, L. J. Ellison, M. Marechal, D. J. Cleaver and G. E. Schröder-Turk, *Interface Focus*, 2017, **7**, 20160161.
- 74 T. H. Epps, E. W. Cochran, T. S. Bailey, R. S. Waletzko, C. M. Hardy and F. S. Bates, *Macromolecules*, 2004, **37**, 8325–8341.
- 75 S. Andersson, S. Hyde, K. Larsson and S. Lidin, *Chem. Rev.*, 1988, **88**, 221–242.
- 76 P. J. Gandy, S. Bardhan, A. L. Mackay and J. Klinowski, *Chem. Phys. Lett.*, 2001, **336**, 187–195.
- 77 H. Von Schnering and R. Nesper, *Z. Phys. B:Condens. Matter*, 1991, **83**, 407–412.
- 78 M. Wohlgemuth, N. Yufa, J. Hoffman and E. L. Thomas, *Macromolecules*, 2001, **34**, 6083–6089.
- 79 O. Al-Ketan and R. K. Abu Al-Rub, *Adv. Eng. Mater.*, 2019, **21**, 1900524.
- 80 J. H. Moon, Y. Xu, Y. Dan, S.-M. Yang, A. T. Johnson and S. Yang, *Adv. Mater.*, 2007, **19**, 1510–1514.
- 81 E. Parzen, *Ann. Math. Stat.*, 1962, **33**, 1065–1076.
- 82 R. A. Davis, K.-S. Lii and D. N. Politis, *Selected Works of Murray Rosenblatt*, Springer, 2011, pp. 95–100.
- 83 P. J. F. Gandy and J. Klinowski, *Chem. Phys. Lett.*, 2000, **321**, 363–371.
- 84 M. Ester, H.-P. Kriegel, J. Sander and X. Xu *et al.*, *KDD*, 1996, pp. 226–231.
- 85 W. E. Lorensen and H. E. Cline, *Seminal Graphics: Pioneering Efforts That Shaped the Field*, Morgan Kaufmann, 1998, pp. 347–353.

